ACS OMEGA

http://pubs.acs.org/journal/acsodf

Article

Ultrahigh Content Boron and Nitrogen Codoped Hierarchically Porous Carbon Obtained from Biomass Byproduct Okara for Capacitive Deionization

Weiqing Kong,* Xu Ge, Qingao Zhang, Yurui Wang, Yueli Wang, Jingyi Lu, Meng Zhang, Desheng Kong, and Yuanyuan Feng*

Cite This: *ACS Omega* 2022, 7, 48282−48290

Read Online

ACCESS | Metrics & More | Article Recommendations | Supporting Information

ABSTRACT: Capacitive deionization (CDI) is an environmentally friendly, energy efficient, and low cost water purification technique in comparison with other conventional techniques, and it has attracted considerable attention in recent years. Here, we use biomass byproduct okara as the starting material to fabricate a boron and nitrogen codoped hierarchically porous carbon (BNC) with ultrahigh heteroatom contents and abundant in-plane nanoholes for CDI application. With the interconnected hierarchical porous structure, the BNC not only exhibits a large surface area (647.0 m^3 g^{-1}) for the adsorption of ions but also offers abundant ion transport channels to access the entire internal surface. Meanwhile, the ultrahigh dopants' content of B (11.9 at%) and N (14.8 at%) further gives rise to the increased surface polarity and enhanced capacitance for BNC. Owing to these favorable properties, BNC exhibits top-level salt adsorption capacity (21.5 mg g^{-1}) and charge efficiency (59.5%) at the initial NaCl concentration of ∼500 mg L^{-1}. Moreover, we performed first-principle simulations to explore the different effects between N-doping and N,B-codoping on the capacitive property, which indicate that the boron and nitrogen codoping of carbon can largely increase the quantum capacitance over the double layer capacitance. The results of this work suggest a promising prospect for the BNC material in practical CDI application.

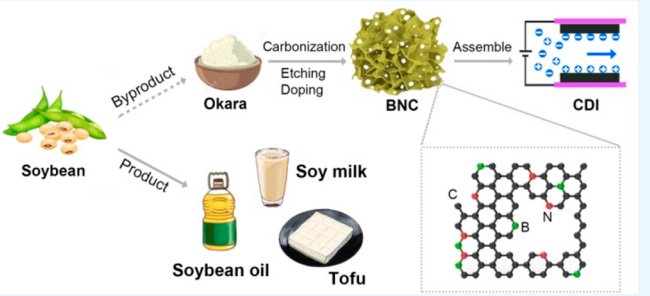

1. INTRODUCTION

Capacitive deionization (CDI) has been burgeoning as an attractive desalination technology in recent years for the treatment and purification of brackish water.[1,2] The CDI process consists of two basic steps. When applying an electric current or voltage on the CDI system, cations and anions move toward the oppositely charged porous electrodes and adsorb on their surface, which establishes the electric double layer (EDL) at the electrode surface and realizes the removal of ions from salt solution. When the external voltage is removed or inverted, the adsorbed ions are released from the electrodes into the solution, while the electrodes are regenerated.[3] It is crucial to rationally design and synthesize electrode materials for optimizing the performance of a CDI system. Various types of carbon materials (such as activated carbon,[4,5] carbon nanotubes,[6,7] and graphene[8,9]), owning high conductivity, low cost, easy availability, large surface area, and excellent chemical stability, have been regarded as the most important electrode materials in the CDI system.[10,11]

The fabrication strategies for carbon materials can be considered from two main aspects. First, fabrication of high-surface-area carbon materials with reasonable porosity or pore size distribution is the prerequisite for achieving high salt adsorption capacity and fast ion transportation kinetics.[12] Recent studies have demonstrated that unimodal micropores distributed in carbon materials are unfavorable for the efficient diffusion of ions.[13,14] Therefore, hierarchically porous carbon materials with a multiporosity structure have recently gained much attention. Specifically, micropores can prominently increase the specific surface area and thus the salt adsorption capacity, because high surface area provides more active sites for ion adsorption.[15,16] Meanwhile, mesopores, especially the ones with a dimension of 2−7 nm, provide the other key characteristics for EDL formation and for a high-performance CDI electrode.[17−19] This is because such mesopores are large enough for accommodating the hydrated electrolyte ions and can serve as an ion-buffering reservoir for facilitating ion transport from larger pores into the inter micropores by shortening ion transport pathways. So, the hierarchical distribution of micropores (<2 nm) along with small sized

Received: October 5, 2022
Accepted: November 29, 2022
Published: December 14, 2022

https://doi.org/10.1021/acsomega.2c06449
ACS Omega 2022, 7, 48282−48290

mesopores (<10 nm) in carbon-based materials could be extremely beneficial for balancing between the salt adsorption capacity and the mass transfer rate during CDI process. Second, heteroatom doping of carbon can effectively boost the CDI capability by introducing additional psudocapacitance to the overall capacitance, improving the electroconductivity of the electrode, and enhancing interfacial interaction between the electrode and electrolyte.[20] The effect of N doping on promoting CDI performance of graphene was first demonstrated in 2015.[21] Since then lots of N-doped carbon materials have been most extensively investigated for their use as CDI electrodes.[22−31] Furthermore, it was also reported that simultaneous doping of N with other heteroatoms into carbon materials is more favorable for promoting the salt adsorption capability of carbon materials. Wang et al. constructed a B, N codoped graphene xerogel with a 1.54 at% B and 8.72 at% N doping via a simple sol−gel method. The as-synthesized material displays significantly enhanced salt adsorption capability (18.45 mg g^{-1}) versus pristine graphene xerogel (13.32 mg g^{-1}).[32] Huo et al. prepared a P, N codoped porous carbon framework with 1.58 at% P and 2.94 at% N doping by a two-step carbonization-activation process. They demonstrated that the dual doping of N and P has a positive influence on the distribution of electron density in carbon, which is greatly beneficial for achieving the high salt adsorption capability (19.3 mg g^{-1}).[33] Generally speaking, a higher heteroatom content tends to provide more polarized surface and introduce additional pseudocapacitance, and thus, is greatly beneficial for yielding a high specific capacitance or salt adsorption capability.[34,35] After a survey of the related literature, it was noticed that in most cases, the total heteroatom content in either single- or multiple-heteroatom doped carbon materials is below 10 at%. Meanwhile, it was lack of a fundamental understanding for realizing the promotion effect of dual heteroatom-codoping in CDI performance.

Porous carbon materials can be fabricated from various natural or synthetic carbonaceous precursors via carbonization-activation methods.[36] In recent years, biomass has been regarded as promising precursors, because they are not only low cost, nontoxic and carbon-rich but also contain plenty of intrinsic hierarchical nanopores, making them suitable for CDI applications.[37,38] For example, Kim et al. developed porous carbon from sorghum with a specific surface area of 1347 m^2 g^{-1} via etching process and carbonization treatments. The porous carbon exhibited good desalination performance of 29.4 mg g^{-1} for CDI.[39] Lu et al. prepared hierarchically porous carbon nanoflakes from xylose, providing a large specific surface area of 408 m^2 g^{-1} and showing a salt adsorption capability of 16.29 mg g^{-1}.[40] More importantly, some of the biomass naturally contain abundant heteroatoms (such as N, S, P atoms), being suitable for preparing heteroatom-doped porous carbon materials. Among these materials, okara, as a byproduct in the manufacturing process of tofu, soya milk, and soya oil, has been produced with annual output in the billions of tons. It is unfortunate that most of them will be burned directly, which will aggravate the deterioration of the ecological environment. Okara is composed of 34.3% crude protein, 11.8% crude fat, 6.7% crude fiber, and 3.6% total high protein content,[41] making it a good starting material for obtaining highly N-doped carbon materials.

Herein, we fabricated a B- and N- codoped, hierarchically porous carbon (BNC) as an electrode material for CDI application (Scheme 1). During the pyrolysis and carbonization process, both appropriate porous structure and B and N codoping can be achieved simultaneously. On the one hand, $ZnCl_2$ is an efficient porogen or etching agent for producing both micro- and meso-pores on the carbon surface.[42] On the other hand, the decomposition of okara and H_3BO_3 can release plentiful gasification molecules, which can not only open the closed pores and further broaden the range of pore distributions but also provide abundant B and N doping elements into the carbon matrix. Originating from the above synergetic porosity and codoping effect, the synthesized BNC, with a reasonable porous structure (ca. 3:1 area ratio for micro- to meso-pores) and ultrahigh heteroatom content (>10 at% for B and N), shows a high specific capacitance, fast ion transport kinetics, large salt adsorption capacity, and excellent adsorption−desorption cycling stability. And to deeply understand the difference between N-doped and N,B-codoped carbon, we evaluated the doping effects on the DOS and quantum capacitance by performing first-principle simulations.

Scheme 1. Schematic Showing the Preparation of BNC and the Process of CDI Desalination

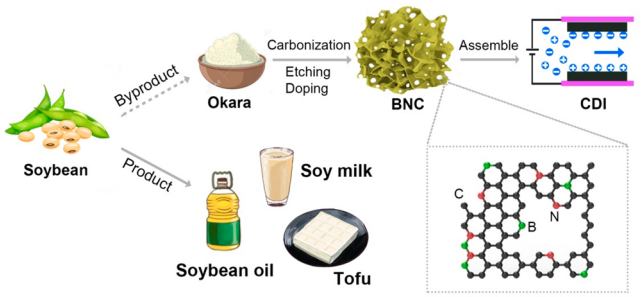

2. EXPERIMENTAL SECTION

2.1. Preparation of BNC and NC. For the synthesis of BNC, the dried okara was first ground in a pestle and then passed through a 20 mesh sieve, obtaining the precursor in powder form. Boric acid (1.0 g), $ZnCl_2$ (1.0 g), and okara powder (1.0 g) were respectively added into deionized water (50 mL). After heating in a water bath with magnetic stirring at 80 °C for 1 h, the obtained concoction suspension was centrifuged at 5000 rpm and freeze-dried to achieve the fluffy products. Then, the fluffy products were sonicated at 800 °C for 2 h (Ar atmosphere, 5 °C min^{-1}). Subsequently, the collected dark solid powder was soaked in 1 M HCl solution with a magnetic stirring for 2 h to remove soluble salts and generated metal nanoparticles. After centrifuging, washing thoroughly with water, and drying in an oven overnight, the BNC was obtained. For comparison, N-doped porous carbon (NC) was synthesized following the similar procedure for BNC, only except that boric acid was not used.

2.2. Characterization. Surface morphology and microstructure of NC and BNC were characterized by scanning electron microscopy (SEM, Zeiss, Germany) and transmission electron microscopy (TEM, JEOL, Japan). The crystal structure and defect degree of the materials were identified via X-ray diffraction (XRD, Shimadzu, Japan) and Raman spectroscopy (Thermo Fisher Scientific, America), respectively. The nitrogen adsorption−desorption isotherms were measured at 77 K using an ASAP 2020 absorption apparatus (Micromeritics, America). Brunauer−Emmett−Teller (BET) model and Barrett−Joyner−Halenda (BJH) model were used to determine the corresponding specific surface area and pore

https://doi.org/10.1021/acsomega.2c06449
ACS Omega 2022, 7, 48282−48290

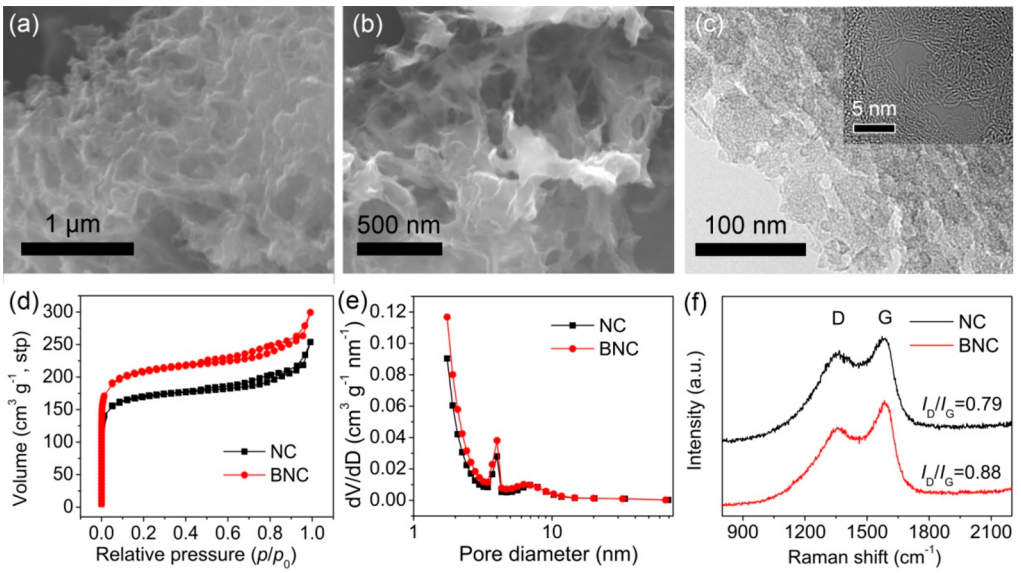

Figure 1. (a, b) SEM images and (c) TEM images for BNC. Inset of (c) shows the HRTEM of BNC. (d) N_2 adsorption−desorption isotherms, (e) the pore size distributions, and (f) Raman spectra for NC and BNC.

size distributions for the samples, respectively. X-ray photoelectron spectroscopy (XPS, ThermoFisher-VG Scientific, USA) was used to characterize the elemental composition and corresponding bonding states in BNC and NC. All XPS spectra had been adjusted by C 1s (284.8 eV).

2.3. Electrochemical and CDI Tests. To prepare the electrode, BNC or NC, acetylene black, and polyvinylidene fluoride with the weight ratio of 8:1:1 were ground in a mortar and then dispersed in *N*-methyl-2-pyrrolidone (NMP) solvent with the aid of a magnetic stirring process. The obtained slurry was subsequently coated onto the surface of a graphite paper with an area of 1 × 1 cm^2. After being desiccated at 80 °C for 1 day in a vacuum oven, the BNC or NC electrode was obtained. The electrochemical features of the samples were investigated using a three-electrode system, in which the prepared electrode, a platinum foil, a saturated calomel electrode (SCE), and 1.0 M NaCl solution were served as working electrode, counter electrode, reference electrode, and electrolyte, respectively. An electrochemical working station (Chenhua, CHI660E) was used to measure cyclic voltammetry (CV) and electrochemical impedance spectroscopy (EIS). Among these methods, EIS spectra were obtained with a frequency range of 100 kHz−0.1 Hz at the open-circuit voltage of 0.3 V. The following equation 1 was used to calculate the specific capacitance *C*.[43]

$$C = \frac{A}{2v \cdot m \cdot \Delta E} \tag{1}$$

where *A*, *v*, *m*, and ΔE are the integral area of the CV curve, the scan rate, the weight of electrode materials loaded, and the potential window, respectively.

CDI desalination performances were investigated using a CDI device (Figure S1), which consists of a CDI cell, a conductivity meter, a potentiostat, and a peristaltic pump. The preparation procedure of CDI electrodes was similar to that of the working electrode for electrochemical measurements. The total mass and the geometric area of the loaded electrode materials on the graphite paper are 40 mg and 20 cm^2, respectively. The CDI experiments were conducted with using 30 mL NaCl solution, 25 mL min^{-1} flow rate, 1.2 V operating voltage. The variation of NaCl concentration was evaluated by a conductivity meter (SevenExcellence Cond meter). The electrosorption capacity (Q) and charge efficiency (Λ) were respectively calculated using equations 2 and 3.[44]

$$Q = \frac{(c_0 - c_e) \cdot V}{m} \tag{2}$$

$$\Lambda = \frac{(c_0 - c_e) \cdot V \cdot F}{M \cdot \int i \cdot dt} \times 100\% \tag{3}$$

where, c_0 and c_e are the concentration of NaCl solution at the initial and equilibrium stage, respectively; *V*, *F*, *M*, *i* and *t* are the volume of the NaCl solution, Faraday constant, molar mass of NaCl, current density, and time during CDI process, respectively.

3. RESULTS AND DISCUSSION

The detailed nanostructures of BNC and NC are analyzed by SEM and TEM studies. SEM images in Figure 1a and 1b reveal that the BNC presents a honeycomb-like porous framework, consisting of few-layer graphene-like carbon nanosheets and abundant submicron level macropores ranging from 50 to 200 nm. Compared with BNC, NC displays a slightly textured morphology (Figure S2), the BNC shows a relatively fluffier surface structure. This is ascribed to the decomposition of H_3BO_3 to produce HBO_2, B_2O_3, and H_2O gases during annealing process, which act as "nanobombs" to expand the local space and create more pores. Furthermore, from the TEM images of BNC shown in Figure 1c, it can be seen that abundant in-plane nanoholes with the pore size around 4−10 nm distributed across the whole basal plane due to $ZnCl_2$ chemical etching of the carbon sheets. The in-plane nanoholes can increase the specific surface areas and provide efficient ion transport channels to reduce ion transport distance between carbon sheets, which were proved in our previous works.[43]

Multiple techniques have been employed to analyze the porous structure and chemical composition of the BNC and NC. Figure 1d presents the nitrogen adsorption−desorption isotherms for BNC and NC, exhibiting a combined feature of

https://doi.org/10.1021/acsomega.2c06449
ACS Omega 2022, 7, 48282−48290

type I and IV isotherms.[45] The coexistence of micro-, meso-, and macro-pores in BNC and NC can be demonstrated by the rapid increase at $P/P_0 < 0.01$, distinct hysteresis between 0.45 and 0.9 (P/P_0) and slow increase at $P/P_0 > 0.9$. Figure 1e displays both ~1.5 nm micropores and 4−7 nm mesopores that are predominant in BNC and NC, and the ratio of micro- to meso-pore surface areas was estimated as ~3 for both materials (Table S1). The similarity in the pore size distribution for NC and BNC results from the effect of $ZnCl_2$ porogen during carbonization process. However, BNC demonstrates higher BET surface area (647.0 $m^2\ g^{-1}$), pore volume (0.46 $cm^3\ g^{-1}$), micropore (489.3 $m^2\ g^{-1}$), and mesopore (157.7 $m^2\ g^{-1}$) surface area than those for NC (Table S1), consistent with the above SEM observations. XRD and Raman spectra illuminate the disordered feature of the BNC and NC. The XRD patterns show two diffraction peaks at $2\theta \approx 26.4°$ and 44.3° (Figure S3), which are indexed to the (002) and (101) lattice planes of graphite (PDF#41-1487). These diffraction peaks are very broad, indicating both samples consisted of a mixture of amorphous, turbostratic, and graphitic carbon phases.[46,47] The Raman spectra further reveals the difference in defect degree between NC and BNC. Figure 1f shows two characteristic peaks at ~1336 cm^{-1} (D band) and 1578 cm^{-1} (G band), which correspond to the structural defects and the crystalline graphite, respectively. The intensity ratio of D band to G band (I_D/I_G) can be used for evaluating the defect degree in carbon-based materials.[44] So, the increased I_D/I_G value from 0.79 for NC to 0.88 for BNC indicates that further introducing heteroatoms (i.e., B atoms) into the carbon matrix could increase the number of defective sites. This may be accompanied both by the opening of closed pores and by the creation of new small pores inside NC, leading to a 20 ± 3% increase in the pore volume as well as in specific surface area from NC to BNC (Table S1).

XPS in combination with element mappings of SEM was performed to achieve insight into the elemental composition and corresponding bonding states in BNC and NC. Figure 2a shows the XPS survey spectra, where BNC presents four peaks at 190 eV (B 1s), 284 eV (C 1s), 400 eV (N 1s), and 532 eV (O 1s), respectively. The content for B and N is determined to be 11.9 and 14.8 at% by integrating the corresponding peak area. The ultrahigh heteroatom content is attributed to two features: (1) the okara is rich in the protein, which provides abundant nitrogen element for self-doping during annealing process. As is in case of NC, without the addition of H_2BO_3, it still maintains an ultrahigh N-doping content of 11.4 at% (Figure S4); (2) boron atom is easy to dope into the carbon matrix, since the bond energy of B−C (448 kJ mol^{-1}) is higher than that of C−C (335 kJ mol^{-1}) yet with comparative bond lengths (156 pm for B−C bond and 154 pm for C−C). Figure 2b and 2c show the high-resolution N 1s and B 1s spectra for BNC, respectively, and the corresponding content are calculated from the deconvoluted XPS spectra and summarized in Table S2. After curve fitting for N 1s spectra, the peaks at binding energy of 397.4, 398.1, 399.3, and 400.8 eV are ascribed to pyridine nitrogen, C−N−B, pyrrolic nitrogen, and graphitic nitrogen, respectively.[33,48] And the fitted B 1s presents the peaks at 190.2 and 191.3 eV, resulting from the responses of B−C and B−N bonds.[32,49] As shown in Figure 2d, the corresponding SEM image and elemental mappings demonstrate the uniform distribution of B and N elements within BNC nanosheets. The combination of the multiscale pore structure and B,N-codoping is expected to render BNC a promising electrode material for ion adsorption/removal from salt solutions.

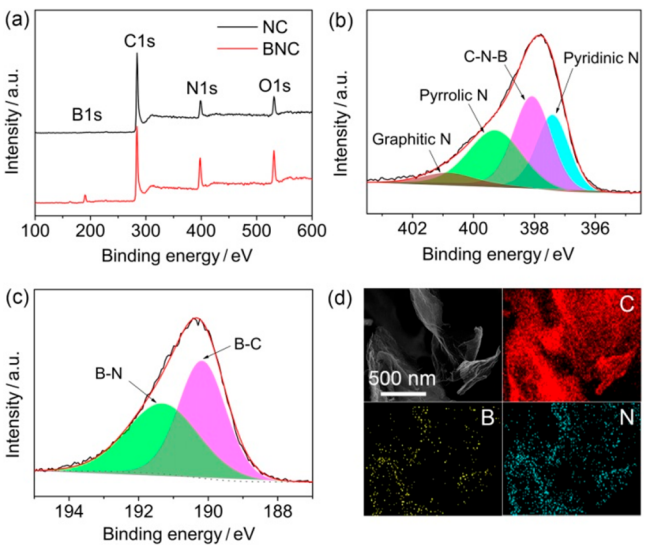

Figure 2. (a) XPS spectrum of NC and BNC. High-resolution XPS spectra of N 1s peak (b) and B 1s peak (c) in the BNC. (d) SEM and elemental mappings of BNC.

The capacitive behaviors of NC and BNC electrodes are systematically tested by performing CV and EIS measurements in 1 M NaCl solution using a standard three electrode system. The CV curves of BNC and NC are evaluated at a range of potentials from −0.3 to 0.7 V. Figure 3a depicts both curves exhibit nearly symmetric and rectangular patterns, indicating a nearly ideal EDL charge−discharge behavior. In comparison with NC, the BNC reveals a higher integral area of CV curve, which is indicative of a higher capacitance of BNC owing to high specific surface area and B, N codoped effect. When the scan rate is increased from 2 to 100 mV s^{-1}, the CV curves of BNC can maintain the symmetric and rectangular profiles under all used scan rates, demonstrating its good rate capability and laudably capacitive nature (Figure 3b). In contrast, the CV curve of NC exhibits a slight distortion when the scan rates above 50 mV s^{-1} (Figure S5), indicating an ion-diffusion controlled kinetics for the EDL formation at higher scan rates.[50] This is because ions have no sufficient time to diffuse into the porous structures at higher scan rates, delaying the formation of EDL.[51] The overall correlation between current (I) and scan rate (ν) is identified according to the equation $I = a\nu^b$,[52] where a and b are constants. There are two well-defined boundary conditions, $b = 1$ and $b = 0.5$. The former indicates a fast surface charge storage or transport process free of diffusion control, while the later means a slow ion-diffusion controlled kinetics. Figure S6 shows the log$I$−logν plots for BNC and NC electrodes at 0.0, 0.2, and 0.4 V. By performing linear fittings, the b value was estimated as 0.83 for BNC and 0.77 for NC, respectively, suggesting the relatively faster charge storage for BNC, or alternatively, the slower ion diffusion for NC. The CV features indicate that BNC possesses a favorable porous structure for rapid ion storage. As a result, the BNC exhibits higher specific capacitance than NC at any scan rate (Figure 3c) and even achieves a remarkable capacitance of 174.2 F g^{-1} at 2 mV s^{-1}. The stability of the BNC was tested with repeated 200 CV cycles (Figure 3d). With the almost unchanged CV

https://doi.org/10.1021/acsomega.2c06449
ACS Omega 2022, 7, 48282−48290

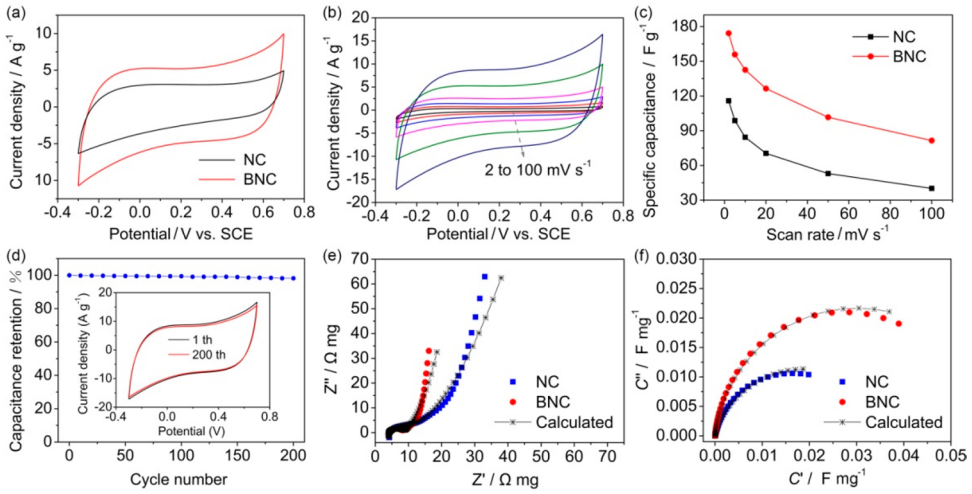

Figure 3. (a) CV curves of NC and BNC at a scan rate of 50 mV s^{-1}. (b) CV curves of BNC at various scan rates. (c) Comparison of specific capacitances vs different scan rates. (d) Cycling stability of BNC at 50 mV s^{-1} with inset showing the CV curves from 1th to 200th cycles. (e) Measured and fitted EIS spectra and (f) normalized capacitance versus frequency for the BNC materials.

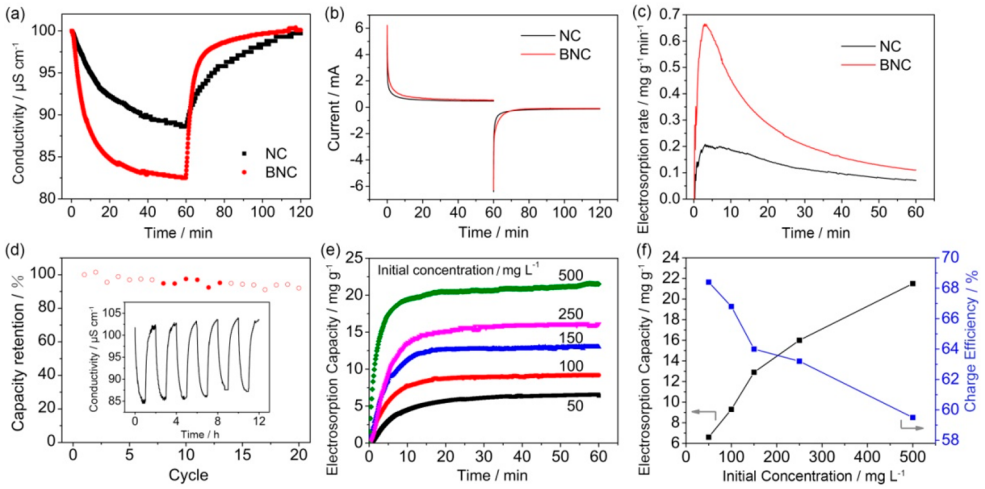

Figure 4. CDI performance tests. (a–c) Plots of conductivity (a), current (b), and desalination rate (c) variations CDI time for NC and BNC electrodes in a 50 mg L^{-1} NaCl solution. (d) The regeneration performance for BNC electrode in a 50 mg L^{-1} NaCl solution. Inset shows the conductivity changes in the NaCl solution during 8–13 cycles. (e) The electrosorption capacity curves for BNC electrode in different initial concentrations of NaCl solutions (from 50 to 500 mg L^{-1}). (f) Plot of electrosorption capacity and charge efficiency vs initial NaCl concentration for BNC electrode.

curve shapes, the capacitance retention is nearly 100%, indicating satisfactory adsorption–desorption stability.

To understand the improved capacitive ion storage at BNC/solution interface, we further performed EIS studies for NC and BNC materials. Figure 3e and 3f show the Nyquist plots and complex capacitance spectra measured at 0 V. Figure 3e exhibits a small semicircle at high frequencies, a 45° Warburg straight line at middle frequencies, and a nearly vertical capacitive line at low frequencies. While, Figure 3f features a predominant capacitive semicircle, where the obviously larger diameter of BNC indicates a significantly increased low-frequency limiting capacitance. Similar EIS responses were also measured at 0.3 V (Figure S7). To account for such characteristics, the equivalent electrical circuit model shown in Figure S8 was proposed for analyzing the measured EIS spectra. With a comparison of the estimated electrochemical parameters for NC and BNC (Table S3), several reasons can be asserted for the effectively enhanced salt ion removal performance by N,B-codoping. First, the interfacial contact property between carbon particles was mended by N,B-codoping. The relatively smaller contact resistance (R_c) of BNC indicates a better electronic conductance than NC. At the same time, the contact capacitance (C_c, which corresponds to Q-Y_0 in Table S3) of BNC is ca. 1/5 of NC, suggest less parasitic electronic charges at the interface between BNC particles (or alternatively, more electronic charges can be used effectively for adsorbing ions). Second, the ion transport property within the pores of the electrode materials was improved by N,B-codoping. This can be manifested both by the decreased Warburg coefficient (σ) from ~21 Ω mg $s^{-1/2}$ (at 0 V) for NC to ~8 Ω mg $s^{-1/2}$ for BNC, and by the decreased diffusion resistance (R_D) from ~57 Ω mg for NC to ~19 Ω mg for BNC. Third, N,B-codoping can accelerates the rate for the charge/discharge process within the EDL. The higher values of characteristic frequency (ω_0) for NC (<1 Hz) indicate a slower ion storage/withdrawing process (>1 s). In

https://doi.org/10.1021/acsomega.2c06449
ACS Omega 2022, 7, 48282–48290

contrast, ω_0 > 1 Hz for BNC indicate a faster process (<1 s) for completing the ion adsorption/desorption. As a result of the superior figure of merits due to N,B-codoping, BNC (relative to NC) delivers a ∼60% enhancement in the low-frequency limiting capacitance (C_0).

The desalination performance of NC and BNC was tested using a symmetric CDI device. Figure 4a presents the evolution of conductivity vs CDI time for NC and BNC electrodes. With the saline water continuously flowing through the CDI cell under an applied voltage of 1.2 V, the conductivity rapidly decreases within 10 min, and then reaches a fully saturated absorption after ca. 60 and 30 min for NC and BNC electrode, respectively. Correspondingly, the salt adsorption capacity of NC and BNC electrodes is 4.2 and 6.6 mg g^{-1}, respectively. Subsequently, when 0 V is applied, the conductivity gradually returns to the initial value due to the release of the adsorbed ions to the solution. While the charge efficiency, being extracted from the evolution of the transient current vs CDI time (Figure 4b), is 54.2% for NC and 68.4% for BNC, respectively, the maximum desalination rate (0.66 mg g^{-1} min^{-1}) of BNC is 3 times higher than that (0.21 mg g^{-1} min^{-1}) of NC (Figure 4c). The electrosorption and regeneration behavior of BNC electrode is evaluated by tautologically applying the voltage of 1.2 and 0 V for 20 times at an initial concentration of 50 mg L^{-1} (Figure 4d). Clearly, the capacity retention is >90% after 20 adsorption−desorption cycles (40 h), indicating excellent regenerative ability of BNC electrode. The CDI performance of BNC was further evaluated by altering the initial concentration of NaCl solution from 50 to 500 mg L^{-1} (Figure 4e). It can be seen from Figure 4f that the electrosorption capacity and charge efficiency of BNC gradually change from 6.6 mg g^{-1} and 68.4% to 21.5 mg g^{-1} and 59.5%. The higher NaCl concentrations usually lead to the easier formation of EDL on the surface of electrodes, which benefits to increase the electrosorption capacity of CDI. Meanwhile, the reduction of charge efficiency is attributed to the increased co-ion expulsion effect with increasing initial NaCl concentration.[53] Table S4 summarizes and compares the heteroatom contents, structural features, and CDI performance for various carbon-based materials reported in the literature and the BNC invested in this work. As is seen from Table S4, the BNC exhibits a higher electrosorption capacity than most traditional carbon materials and biomass-derived carbons. Two factors may be responsible for the better desalination performances. First, the high specific surface area and large pore volume of BNC could provide plenty of active sites to adsorb the ions. Meanwhile, the reasonable pore size distributions of both <2 nm micropores and 3−8 nm mesopores can well match with the theoretical calculation results for the optimum pore dimension (<5 nm),[54,55] which are favorable both for the ion adsorption and for ion diffusion processes within BNC. Second, comparing with other single- or multielement doped carbon materials, BNC possesses the ultrahigh contents of N and B atoms, which can notably increase the electronic conductance, surface polarity, and charge/discharge rate for the charge storage process within EDL.

For deeply understanding the benefit of N,B-codoping for enhancing the capacitance and thus for increasing the electrosorption capacity, we also performed density function theory (DFT) calculations. For this purpose, graphene sheets can be used as a mimic model to exploring the electronic and electrochemical properties for carbon-based materials.[56,57] Figure 5a and 5b show the atomic models used for calculations, which were constructed with the substitute of

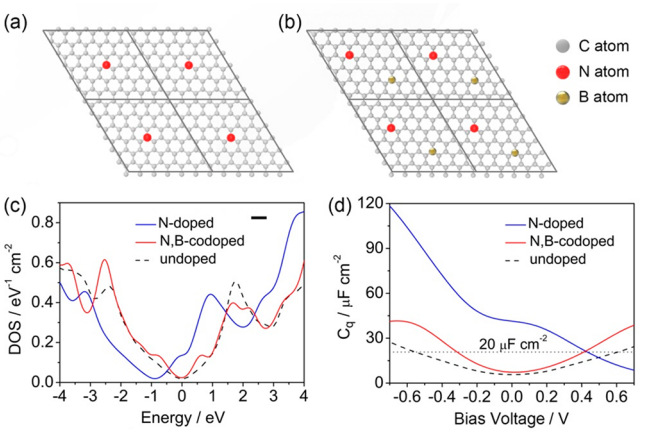

Figure 5. Atomic models of (a) N-doped and (b) N,B-codoped graphene sheet with 6 × 6 supercells, and the calculated density of state (c) and quantum capacitance (d). In panel (a) and (b), the N and B atoms are shown respectively in blue and pink, while the black lines indicate the periodic boundaries. In (c) the Fermi level is set to zero, and in (d) the typical value for Helmholtz double layer capacitance (C_H ∼ 20 μF cm^{-2}) is indicated with a dotted horizontal line.

nitrogen or boron atom for carbon atom to simulate the N-doping and N,B-codoping of the hexagonal carbon network. In these calculations, the Perdew−Burke−Ernzerhof (PBE) exchange-correlation functional[58] of generalized gradient approximation was adopted by using the CASTEP module of Materials Studio.[59] A vacuum region of 20 Å along the z direction was added to avoid the interaction between graphene sheets, and a 12 × 12 × 1 k-points Monkhorst−Pack grid was used for calculating the density of states (DOS). The calculated DOS curves (Figure 5c) clearly manifest that while N-doping shifts up the Fermi level (by ∼0.9 eV) of graphene sheet from the Dirac point, it remains almost *unchanged* for N,B-codoping. This may be because the substitution of a carbon atom with a nitrogen atom increases the number of π elections in the carbon network, leading to an n-type electronic doping effect.[50] In contrast, as boron atom is short of one 2p election relative to carbon, the incorporation of both nitrogen and boron atoms in graphene sheets does not change the total number of π elections, leading to a compensation and/or complementation effect of N,B-codoping. However, in both cases, the DOS near the Fermi level (within ±1 eV) is obviously larger than that of undoped graphene sheet.

From the obtained DOS, we further evaluated the quantum capacitance based on the assumption of fixed band approximation.[60] Under an applied bias potential (ϕ), the electrochemical potential (μ) of an electrode material is rigidly shifted by $e\phi$, leading to the estimation of the excess charge (Q) and thus of the quantum capacitance (C_q).[60,61] It is described based on the below equations 4 and 5:

$$Q = e\int_{-\infty}^{\infty} D(E)[f(E) - f(E-\mu)]\mathrm{d}E \tag{4}$$

$$C_q = \frac{\mathrm{d}Q}{\mathrm{d}\phi} = \frac{e^2}{4kT}\int_{-\infty}^{\infty} D(E)\mathrm{sech}^2\left(\frac{E-\mu}{2kT}\right)\mathrm{d}E \tag{5}$$

https://doi.org/10.1021/acsomega.2c06449
ACS Omega 2022, 7, 48282−48290

where $D(E)$ is the DOS, E is the energy relative to Fermi level, $f(E)$ is the Fermi−Dirac distribution function, $f(E) = 1/[1+\exp(E/kT)]$, and T is temperature (300 K). Figure 5d shows the theoretical quantum capacitance for undoped, N-doped, and N,B-codoped graphene sheets. In principle, the total capacitance (C_{total}) for carbon-based electrode materials is contributed both from the Helmholtz double layer capacitance (C_H) and from C_q (with $1/C_{total} = 1/C_H + 1/C_q$),[62] and thus, is dominated by the smaller one of the two. A typical value for C_H is 20 μF cm^{-2},[62] which is indicated as a reference in Figure 5d. The results clearly demonstrate that, within the bias voltage window from −0.6 to 0.6 V, the C_q of the undoped graphene sheet is less than C_H. In contrast, the N-doping can significantly level up C_q at negative biases, but it gradually decreases C_q at positive biases ($C_q < C_H$ above 0.4 V). This means that although the N-doped carbon is very suitable for its use as the cathode material in CDI system, the total capacitance is still limited by the rather low quantum capacitance at the anode. However, in the case of N,B-codoping, $C_q > C_H$, both at the negative biases (<−0.3 V) and at the positive biases (>0.4 V). So, under 1.2 V applied voltage in CDI (as is used in this work), the bottleneck effect of the quantum capacitance limited total capacitance can be overcome. Because C_q depends only on the intrinsic nature of an electrode material, this result provides a theoretical insight for recognizing the enhanced capacitance and CID properties of BNC relative to that of NC.

4. CONCLUSION

In summary, an ultrahigh content N and B heteroatom codoped hierarchically porous carbon (BNC) was successfully synthesized from biomass byproduct okara. It was demonstrated that by using okara as C and N source, boric acid as B source, and $ZnCl_2$ as porogen, effective carbonization, N,B-codoping, and etching can be achieved by a single step of annealing treatment at a moderate temperature (800 °C). This material consists of few-layer graphene-like carbon sheets and is rich in both <2 nm micropores and 3−8 nm mesopores. Owing to its multiscale porous structure, superior specific surface area, and the N,B-codoping effect, BNC exhibits an enhanced electrochemical activity for salt removal, with an extremely high CDI desalination capacity of 6.6 and 21.5 mg g^{-1} in 50 and 500 mg L^{-1} NaCl solution, respectively, and an excellent cycling stability over 20 cycles. Theoretical calculations indicate that N and B codoping of carbon can contribute more DOS around the Fermi level and level up effectively the quantum capacitance under both positive and negative biases. In contrast, N-doped carbon is only suitable for its use as a cathode material for CDI because of its rather low quantum capacitance at positive bias. Due to the possibility of scalable synthesis and inexpensive precursors, the BNC is believed to be a promising candidate for the applications in desalination, catalysis, energy storage, and other fields.

■ ASSOCIATED CONTENT

Supporting Information

The Supporting Information is available free of charge at https://pubs.acs.org/doi/10.1021/acsomega.2c06449.

SEM, XPS, and CV curves of NC; XRD, logarithmic current versus scan rate diagrams, Nyquist plots, complex capacitance spectra, and equivalent electrical circuit for BNC and NC; summary of specific surface area and pore-size distributions of NC and BNC; summary of specific surface area and pore-size distributions of NC and BNC; atomic percentages of various elements N 1s of NC and N 1s and B 1s of BNC; electrochemical equivalent electrical circuit parameters estimated for NC and BNC electrodes; comparison of the CDI performance for different carbon materials (PDF)

■ AUTHOR INFORMATION

Corresponding Authors

Weiqing Kong − *College of Chemistry and Chemical Engineering, Qufu Normal University, Qufu, Shandong 273165, PR China*; orcid.org/0000-0002-3203-6919; Email: hxkwq3069@163.com

Yuanyuan Feng − *College of Chemistry and Chemical Engineering, Qufu Normal University, Qufu, Shandong 273165, PR China*; orcid.org/0000-0003-2078-0086; Email: fengyy@qfnu.edu.cn

Authors

Xu Ge − *College of Chemistry and Chemical Engineering, Qufu Normal University, Qufu, Shandong 273165, PR China*

Qingao Zhang − *College of Chemistry and Chemical Engineering, Qufu Normal University, Qufu, Shandong 273165, PR China*

Yurui Wang − *College of Chemistry and Chemical Engineering, Qufu Normal University, Qufu, Shandong 273165, PR China*

Yueli Wang − *College of Chemistry and Chemical Engineering, Qufu Normal University, Qufu, Shandong 273165, PR China*

Jingyi Lu − *College of Chemistry and Chemical Engineering, Qufu Normal University, Qufu, Shandong 273165, PR China*

Meng Zhang − *College of Chemistry and Chemical Engineering, Qufu Normal University, Qufu, Shandong 273165, PR China*

Desheng Kong − *College of Chemistry and Chemical Engineering, Qufu Normal University, Qufu, Shandong 273165, PR China*

Complete contact information is available at: https://pubs.acs.org/10.1021/acsomega.2c06449

Author Contributions

The manuscript was written through contributions of all authors. All authors have given approval to the final version of the manuscript.

Notes

The authors declare no competing financial interest.

■ ACKNOWLEDGMENTS

This work is supported by the National Natural Science Foundation of China (22072070) and the Natural Science Foundation of Shandong Province (ZR2019MB036).

■ REFERENCES

(1) Gamaethiralalage, J. G.; Singh, K.; Sahin, S.; Yoon, J.; Elimelech, M.; Suss, M. E.; Liang, P.; Biesheuvel, P. M.; Zornitta, R. L.; de Smet, L. C. P. M. Recent advances in ion selectivity with capacitive deionization. *Energy Environ. Sci.* **2021**, *14*, 1095−1120.

(2) Li, Q.; Xu, X. T.; Guo, J. R.; Hill, J. P.; Xu, H. S.; Xiang, L. X.; Li, C.; Yamauchi, Y.; Mai, Y. Y. Two-dimensional MXene-Polymer heterostructure with ordered in-plane mesochannels for high-performance capacitive deionization. *Angew. Chem., Int. Ed.* **2021**, *60*, 26528−26534.
(3) Wang, H.; Chen, B. H.; Liu, D. J.; Xu, X. T.; Osmieri, L.; Yamauchi, Y. Nanoarchitectonics of metal-organic frameworks for capacitive deionization via controlled pyrolyzed approaches. *Small* **2022**, *18*, 2102477.
(4) Chen, Z.; Zhang, H.; Wu, C.; Wang, Y.; Li, W. A study of electrosorption selectivity of anions by activated carbon electrodes in capacitive deionization. *Desalination* **2015**, *369*, 46−50.
(5) Sufiani, O.; Tanaka, H.; Teshima, K.; Machunda, R. L.; Jande, Y. A. C. Enhanced electrosorption capacity of activated carbon electrodes for deionized water production through capacitive deionization. *Sep. Purif. Technol.* **2020**, *247*, 116998.
(6) Zhang, H.; Zhang, F.; Wei, Y. Q.; Miao, Q. C.; Li, A. Y.; Zhao, Y. S.; Yuan, Y.; Jin, N. F.; Li, G. H. Controllable design and preparation of hollow carbon-based nanotubes for asymmetric supercapacitors and capacitive deionization. *ACS Appl. Mater. Interfaces* **2021**, *13*, 21217−21230.
(7) Song, D.; Guo, W.; Zhang, T.; Lu, P.; Guo, A.; Hou, F.; Yan, X.; Liang, J. A freestanding CNTs film fabricated by pyrrole-modified CVD for capacitive deionization. *Surf. Innov.* **2019**, *7*, 10−17.
(8) Yang, Z. Y.; Jin, L. J.; Lu, G. Q.; Xiao, Q. Q.; Zhang, Y. X.; Jing, L.; Zhang, X. X.; Yan, Y. M.; Sun, K. N. Sponge-templated preparation of high surface area graphene with ultrahigh capacitive deionization performance. *Adv. Funct. Mater.* **2014**, *24*, 3917−3925.
(9) Wang, H.; Mi, X. Y.; Li, Y.; Zhan, S. H. 3D graphene-based macrostructures for water treatment. *Adv. Mater.* **2020**, *32*, 1806843.
(10) Zhang, M.; Kong, W. Q. Recent progress in graphene-based and ion-intercalation electrode materials for capacitive deionization. *J. Electroanal. Chem.* **2020**, *878*, 114703.
(11) Zhang, S. H.; Xu, X. T.; Liu, X. H.; Yang, Q.; Shang, N. Z.; Zhao, X. X.; Zang, X. H.; Wang, C.; Wang, Z.; Shapter, J. G.; Yamauchi, Y. Heterointerface optimization in a covalent organic framework-on-MXene for high-performance capacitive deionization of oxygenated saline water. *Mater. Horiz.* **2022**, *9*, 1708−1716.
(12) Shui, P.; Alhseinat, E. Quantitative insight into the effect of ions size and electrodes pores on capacitive deionization performance. *Electrochim. Acta* **2020**, *329*, 135176.
(13) Kim, M.; Xu, X. T.; Xin, R. J.; Earnshaw, J.; Ashok, A.; Kim, J.; Park, T.; Nanjundan, A. K.; El-Said, W. A.; Yi, J. W.; Na, J.; Yamauchi, Y. KOH-activated hollow ZIF-8 derived porous carbon: nano-architectured control for upgraded capacitive deionization and supercapacitor. *ACS Appl. Mater. Interfaces* **2021**, *13*, 52034−52043.
(14) Kim, M.; Firestein, K. L.; Fernando, J. F. S.; Xu, X. T.; Lim, H.; Golberg, D. V.; Na, J.; Kim, J.; Nara, H.; Tang, J.; Yamauchi, Y. Strategic design of Fe and N co-doped hierarchically porous carbon as superior ORR catalyst: from the perspective of nanoarchitectonics. *Chem. Sci.* **2022**, *13*, 10836−10845.
(15) Young, C.; Lin, J. J.; Wang, J.; Ding, B.; Zhang, X. G.; Alshehri, S. M.; Ahamad, T.; Salunkhe, R. R.; Hossain, S. A.; Khan, J. H.; Ide, Y.; Kim, J.; Henzie, J.; Wu, K. C.; Kobayashi, N.; Yamauchi, Y. Significant effect of pore sizes on energy storage in nanoporous carbon supercapacitors. *Chem.—Eur. J.* **2018**, *24*, 6127−6132.
(16) Han, B.; Cheng, G.; Wang, Y. K.; Wang, X. K. Structure and functionality design of novel carbon and faradaic electrode materials for high-performance capacitive deionization. *Chem. Eng. J.* **2019**, *360*, 364−384.
(17) Yeh, C. L.; Hsi, H. C.; Li, K. C.; Hou, C. H. Improved performance in capacitive deionization of activated carbon electrodes with a tunable mesopore and micropore ratio. *Desalination* **2015**, *367*, 60−68.
(18) Kumagai, S.; Sato, M.; Tashima, D. Electrical double-layer capacitance of micro- and mesoporous activated carbon prepared from rice husk and beet sugar. *Electrochim. Acta* **2013**, *114*, 617−626.
(19) Porada, S.; Borchardt, L.; Oschatz, M.; Bryjak, M.; Atchison, J. S.; Keesman, K. J.; Kaskel, S.; Biesheuvel, P. M.; Presser, V. Direct prediction of the desalination performance of porous carbon electrodes for capacitive deionization. *Energy Environ. Sci.* **2013**, *6*, 3700−3712.
(20) Li, Y. Y.; Chen, N.; Li, Z. L.; Shao, H. B.; Qu, L. T. Frontiers of carbon materials as capacitive deionization electrodes. *Dalton T.* **2020**, *49*, 5006−5014.
(21) Xu, X. T.; Pan, L. K.; Liu, Y.; Lu, T.; Sun, Z. Enhanced capacitive deionization performance of graphene by nitrogen doping. *J. Colloid Interface Sci.* **2015**, *445*, 143−150.
(22) Vafakhah, S.; Sim, G. J.; Saeedikhani, M.; Li, X.; Valdivia y Alvarado, P.; Yang, H. Y. 3D printed electrodes for efficient membrane capacitive deionization. *Nanoscale. Advances.* **2019**, *1*, 4804−4811.
(23) Deka, N.; Barman, J.; Kasthuri, S.; Nutalapati, V.; Dutta, G. K. Transforming waste polystyrene foam into N-doped porous carbon for capacitive energy storage and deionization applications. *Appl. Surf. Sci.* **2020**, *511*, 145576.
(24) Li, Y.; Liu, Y. X.; Shen, J. M.; Qi, J. W.; Li, J. S.; Sun, X. Y.; Shen, J. Y.; Han, W. Q.; Wang, L. J. Design of nitrogen-doped cluster-like porous carbons with hierarchical hollow nanoarchitecture and their enhanced performance in capacitive deionization. *Desalination* **2018**, *430*, 45−55.
(25) Amiri, A.; Chen, Y.; Bee Teng, C.; Naraghi, M. Porous nitrogen-doped MXene-based electrodes for capacitive deionization. *Energy Storage Mater.* **2020**, *25*, 731−739.
(26) Li, Y. J.; Liu, Y.; Wang, M.; Xu, X. T.; Lu, T.; Sun, C. Q.; Pan, L. K. Phosphorus-doped 3D carbon nanofiber aerogels derived from bacterial-cellulose for highly-efficient capacitive deionization. *Carbon* **2018**, *130*, 377−383.
(27) Xu, X. T.; Allah, A. E.; Wang, C.; Tan, H. B.; Farghali, A. A.; Khedr, M. H.; Malgras, V.; Yang, T.; Yamauchi, Y. Capacitive deionization using nitrogen-doped mesostructured carbons for highly efficient brackish water desalination. *Chem. Eng. J.* **2019**, *362*, 887−896.
(28) Liu, X. H.; Zhang, S. H.; Feng, G. L.; Wu, Z. G.; Wang, D.; Albaqami, M. D.; Zhong, B. H.; Chen, Y. X.; Guo, X. D.; Xu, X. T.; Yamauchi, Y. Core-shell MOF@COF motif hybridization: selectively functionalized precursors for titanium dioxide nanoparticle-embedded nitrogen-rich carbon architectures with superior capacitive deionization performance. *Chem. Mater.* **2021**, *33*, 1657−1666.
(29) Xu, X. T.; Tang, J.; Kaneti, Y. V.; Tan, H. B.; Chen, T.; Pan, L. K.; Yang, T.; Bando, Y.; Yamauchi, Y. Unprecedented capacitive deionization performance of interconnected iron-nitrogen-doped carbon tubes in oxygenated saline water. *Mater. Horiz.* **2020**, *7*, 1404−1412.
(30) Guo, J. R.; Xu, X. T.; Hill, J. P.; Wang, L. P.; Dang, J. J.; Kang, Y. Q.; Li, Y. L.; Guan, W. S.; Yamauchi, Y. Graphene-carbon 2D heterostructures with hierarchically-porous P,N-doped layered architecture for capacitive deionization. *Chem. Sci.* **2021**, *12*, 10334−10340.
(31) Zhang, Y.; Wu, J. Y.; Zhang, S. H.; Shang, N. Z.; Zhao, X. X.; Alshehri, S. M.; Ahamad, T.; Yamauchi, Y.; Xu, X. T.; Bando, Y. MOF-on-MOF nanoarchitectures for selectively functionalized nitrogen-doped carbon-graphitic carbon/carbon nanotubes heterostructure with high capacitive deionization performance. *Nano Energy* **2022**, *97*, 107146.
(32) Wang, S. S.; Feng, J. W.; Meng, Q. H.; Cao, B.; Tian, G. Y. Study on boron and nitrogen co-doped graphene xerogel for high-performance electrosorption application. *J. Solid State Electr.* **2019**, *23*, 2377−2390.
(33) Huo, S. L.; Zhao, Y. B.; Zong, M. Z.; Liang, B. L.; Zhang, X. L.; Khan, I. U.; Li, K. X. Enhanced supercapacitor and capacitive deionization boosted by constructing inherent N and P external defects in porous carbon framework with a hierarchical porosity. *Electrochim. Acta* **2020**, *353*, 136523.
(34) Kicinski, W.; Szala, M.; Bystrzejewski, M. Sulfur-doped porous carbons: Synthesis and applications. *Carbon* **2014**, *68*, 1−32.

https://doi.org/10.1021/acsomega.2c06449
ACS Omega 2022, 7, 48282−48290

(35) Liu, P.; Yan, T.; Shi, L.; Park, H. S.; Chen, X.; Zhao, Z.; Zhang, D. Graphene-based materials for capacitive deionization. *J. Mater. Chem. A* **2017**, *5*, 13907−13943.
(36) Yin, J.; Zhang, W. L.; Alhebshi, N. A.; Salah, N.; Alshareef, H. N. Synthesis strategies of porous carbon for supercapacitor applications. *Small Methods* **2020**, *4*, 1900853.
(37) Yu, F.; Li, S. Z.; Chen, W. R.; Wu, T.; Peng, C. Biomass-derived materials for electrochemical energy storage and conversion: overview and perspectives. *Energy Environ. Mater.* **2019**, *2*, 55−67.
(38) Elisadiki, J.; Kibona, T. E.; Machunda, R. L.; Saleem, M. W.; Kim, W. S.; Jande, Y. A. C. Biomass-based carbon electrode materials for capacitive deionization: a review. *Biomass Convers. Bior.* **2020**, *10*, 1327−1356.
(39) Kim, M.; Lim, H.; Xu, X. T.; Hossain, M. S. A.; Na, J.; Awaludin, N. N.; Shah, J.; Shrestha, L. K.; Ariga, K.; Nanjundan, A. K.; Martin, D. J.; Shapter, J. G.; Yamauchi, Y. Sorghum biomass-derived porous carbon electrodes for capacitive deionization and energy storage. *Micropor. Mesopor. Mater.* **2021**, *312*, 110757.
(40) Lu, T.; Liu, Y.; Xu, X. T.; Pan, L. K.; Alothman, A. A.; Shapter, J.; Wang, Y.; Yamauchi, Y. Highly efficient water desalination by capacitive deionization on biomass-derived porous carbon nanoflakes. *Sep. Purif. Technol.* **2021**, *256*, 117771.
(41) Yang, T. Z.; Qian, T.; Wang, M. F.; Shen, X. W.; Xu, N.; Sun, Z. Z.; Yan, C. L. A sustainable route from biomass byproduct okara to high content nitrogen-doped carbon sheets for efficient sodium ion batteries. *Adv. Mater.* **2016**, *28*, 539−545.
(42) Jiang, L. L.; Sheng, L. Z.; Chen, X.; Wei, T.; Fan, Z. J. Construction of nitrogen-doped porous carbon buildings using interconnected ultra-small carbon nanosheets for ultra-high rate supercapacitors. *J. Mater. Chem. A* **2016**, *4*, 11388−11396.
(43) Kong, W. Q.; Duan, X. D.; Ge, Y. J.; Liu, H. T.; Hu, J. W.; Duan, X. F. Holey graphene hydrogel with in-plane pores for high-performance capacitive desalination. *Nano Res.* **2016**, *9*, 2458−2466.
(44) Kong, W. Q.; Wang, G.; Zhang, M.; Duan, X. D.; Hu, J. W.; Duan, X. F. Villiform carbon fiber paper as current collector for capacitive deionization devices with high areal electrosorption capacity. *Desalination* **2019**, *459*, 1−9.
(45) Sing, K. S. W. Reporting physisorption data for gas/solid systems with special reference to the determination of surface area and porosity. *Pure. Appl. Chem.* **1985**, *57*, 603−619.
(46) Cao, B.; Liu, H.; Xu, B.; Lei, Y. F.; Chen, X. H.; Song, H. H. Mesoporous soft carbon as an anode material for sodium ion batteries with superior rate and cycling performance. *J. Mater. Chem. A* **2016**, *4*, 6472−6478.
(47) Liu, C. Q.; Zhang, L. Y.; Yuan, X. X.; Li, X.; Wu, Y. T.; Wang, X. F. Effect of ZrC formation on graphitization of carbon phase in polymer derived ZrC-C ceramics. *Materials* **2019**, *12*, 4153.
(48) Huo, S. L.; Ni, W.; Song, X.; Zhang, M. T.; Wang, H.; Li, K. X. Insight from the synergistic effect of dopant and defect interplay in carbons for high-performance capacitive deionization. *Sep. Purif. Technol.* **2022**, *281*, 119807.
(49) Li, Y. Q.; Xu, X. T.; Hou, S. J.; Ma, J. Q.; Lu, T.; Wang, J. C.; Yao, Y. F.; Pan, L. K. Facile dual doping strategy via carbonization of covalent organic frameworks to prepare hierarchically porous carbon spheres for membrane capacitive deionization. *Chem. Commun.* **2018**, *54*, 14009−14012.
(50) Kong, W. Q.; Zhu, J.; Zhang, M.; Liu, Y. Y.; Hu, J. W. Three-dimensional N- and S-codoped graphene hydrogel with in-plane pores for high performance supercapacitor. *Microporous Mesoporous Mater.* **2018**, *268*, 260−267.
(51) Mi, M. J.; Liu, X. J.; Kong, W. Q.; Ge, Y. J.; Dang, W. Q.; Hu, J. W. Hierarchical composite of N-doped carbon sphere and holey graphene hydrogel for high-performance capacitive deionization. *Desalination* **2019**, *464*, 18−24.
(52) Liu, J. L.; Wang, J.; Xu, C. H.; Jiang, H.; Li, C. Z.; Zhang, L. L.; Lin, J. Y.; Shen, Z. X. Advanced energy storage devices: basic principles, analytical methods, and rational materials design. *Adv. Sci.* **2018**, *5*, 1700322.
(53) Yan, T. T.; Xu, B. X.; Zhang, J. P.; Shi, L. Y.; Zhang, D. S. Ion-selective asymmetric carbon electrodes for enhanced capacitive deionization. *RSC Adv.* **2018**, *8*, 2490−2497.
(54) Porada, S.; Borchardt, L.; Oschatz, M.; Bryjak, M.; Atchison, J. S.; Keesman, K. J.; Kaskel, S.; Biesheuvel, P. M.; Presser, V. Direct prediction of the desalination performance of porous carbon electrodes for capacitive deionization. *Energy Environ. Sci.* **2013**, *6*, 3700−3712.
(55) Tan, J.; Li, Z.; Ye, M.; Shen, J. Nanoconfined Space: Revisiting the Charge Storage Mechanism of Electric Double Layer Capacitors. *ACS Appl. Mater. Interfaces* **2022**, *14*, 37259−37269.
(56) Zhan, C.; Neal, J.; Wu, J. Z.; Jiang, D. E. Quantum effects on the capacitance of graphene-based electrodes. *J. Phys. Chem. C* **2015**, *119*, 22297−22303.
(57) Jiang, H.; Gu, J. X.; Zheng, X.; Liu, M.; Qiu, X.; Wang, L.; Li, W.; Chen, Z.; Ji, X.; Li, J. J. E. Defect-rich and ultrathin N doped carbon nanosheets as advanced trifunctional metal-free electrocatalysts for the ORR, OER and HER. *Energy Environ. Sci.* **2019**, *12*, 322−333.
(58) Perdew, J. P.; Burke, K.; Ernzerhof, M. Generalized gradient approximation made simple. *Phys. Rev. Lett.* **1996**, *77*, 3865−3868.
(59) Clark, S. J.; Segall, M. D.; Pickard, C. J.; Hasnip, P. J.; Probert, M. I. J.; Refson, K.; Payne, M. C. First principles methods using CASTEP. *Z. Krist-Cryst. Mater.* **2005**, *220*, 567−570.
(60) da Silva, D. A. C.; Paulista Neto, A. J.; Pascon, A. M.; Fileti, E. E.; Fonseca, L. R. C.; Zanin, H. G. Combined density functional theory and molecular dynamics simulations to investigate the effects of quantum and double-layer capacitances in functionalized graphene as the electrode material of aqueous-based supercapacitors. *J. Phys. Chem. C* **2021**, *125*, 5518−5524.
(61) Paek, E.; Pak, A. J.; Hwang, G. S. A Computational study of the interfacial structure and capacitance of graphene in [BMIM][PF_6] ionic liquid. *J. Electrochem. Soc.* **2013**, *160*, A1−A10.
(62) Xia, J.; Chen, F.; Li, J.; Tao, N. Measurement of the quantum capacitance of graphene. *Nat. Nanotechnol.* **2009**, *4*, 505−509.

https://doi.org/10.1021/acsomega.2c06449
ACS Omega 2022, 7, 48282−48290